

## Numerical simulations of the shear instability and subsequent degeneration of basin scale internal standing waves

Andrew Grace, Marek Stastna, and Francis J. Poulin\*

*Department of Applied Mathematics, University of Waterloo, Waterloo, Ontario, N2L 3G1, Canada*



(Received 8 May 2018; published 14 January 2019)

We present high-resolution simulations of the instability and subsequent breakdown of standing waves, or seiches, in a fluid continuously stratified in the vertical direction. It is well known that such waves can evolve to form nonlinear, dispersive wave trains. When the initial dimensionless amplitude is large, it is possible that a stratified shear instability develops, possibly at the same time as dispersive wave trains. While both dispersion and shear instability serve to move energy from large to small scales, they are fundamentally different. The development into wave trains is nondissipative in nature, and in the asymptotic limit of small but finite amplitude seiches may be described by variants of the Korteweg–de Vries (KdV) equation. Shear instability, on the other hand, yields Kelvin-Helmholtz billows, which in turn provide one of the basic archetypes of transition to turbulence, with greatly increased rates of mixing and viscous dissipation. We discuss how the two phenomena vary as the aspect ratio of the tank and the height of the interface between lighter and denser fluids are changed, highlighting cases where the two phenomena coexist. A quantitative accounting for the evolution of the horizontal modewise decomposition of the kinetic energy of the system in addition to the creation of a semianalytical model of the evolution of the fundamental mode is presented. Finally, the mixing is characterized during the evolution of the seiche, illustrating a fundamental transition that occurs as the aspect ratio is decreased.

DOI: [10.1103/PhysRevFluids.4.014802](https://doi.org/10.1103/PhysRevFluids.4.014802)

### I. INTRODUCTION

The majority of temperate lakes are density stratified throughout a significant portion of the calendar year [1]. While the true interior of a lake is continuously stratified, a reasonable idealization is of two isothermal layers, of thicknesses  $h_2$  (lower) and  $h_1$  (upper), separated by a sharp interface. This interface provides a wave guide, with a reduced gravity proportional to the density change across the layer. This is typically two orders of magnitude smaller than at the air-water interface and hence waves in the interior, or internal waves, are much larger in amplitude and more slowly propagating than waves on the surface. It has been known since as far back as 1904 [2] that the isothermal surfaces in Loch Ness oscillate with a period dependent on physical parameters such as the lake's length and depth. A century of observational work has led to the basic understanding of internal seiches as driven by the wind in the following manner. A sustained period of wind leads to water "piling up" on the downwind side of the lake. While the change in water depth is small, the resulting pressure gradient is large enough so that the compensating displacement of the interior isotherms from their rest height is large (on the order of several meters). When the wind ceases, the sloping internal interface begins to oscillate, yielding large-amplitude standing waves [3]. The

---

\*Corresponding author: [a2grace@uwaterloo.ca](mailto:a2grace@uwaterloo.ca)

standing waves created via the above processes break down into propagating wave trains, which in turn transport material and energy.

Observations of large-amplitude wave trains in lakes have been reported at a wide variety of geographic locations. Lake Kinneret, Israel, has received consistent sampling by multiple groups. Ostrovsky *et al.* [4] provided evidence that the smaller internal wave dynamics induced by a seiche in the lake can mix hypolimnetic and epilimnetic waters while Boegman *et al.* [5] provided a conceptual model of the fate of shoaling internal solitary waves and their ramifications for the bottom boundary layer. Specifically, Boegman *et al.* [5] proposed that due to surface wind forcing, horizontal currents were induced which degenerated into trains of solitary waves, which then shoal on the boundaries of the lake and energize the bottom boundary layer. This process has ramifications for the biomass of the lake because of the vertical transport of organic material that might otherwise not have any way to reach the surface. Large-amplitude trains of internal solitary-like waves (ISWs) have been reported in Lake Constance [6–8]. Strong seasonality [8], episodes of turbulence [6], and internal wave overturning in open water were reported [7]. Finally, MacIntyre *et al.* [9] characterized the nonlinear steepening of internal seiches after the cessation of sustained winds in Mono Lake, finding that over steep slopes (10%) roughly 80% of the water column was turbulent. A very different type of internal motion was documented by Henderson and Deemer [10], who observed vertical propagation of energy in Lake Lacmas, USA, due to internal seiche motion. While the vertical propagation was unique, the bulk behavior was consistent with other observations. Namely, interaction with boundaries drives turbulence production [11] and dissipation of the internal waves themselves. In the bottom boundary layer, enhanced turbulence drives chemical exchange [12].

Internal waves in lakes have been simulated using a variety of numerical models and at different levels of detail. Basin-scale models, for larger lakes especially, typically make the hydrostatic approximation. This is expedient numerically but *a priori* removes short wave dispersion, which is a well-known aspect of internal waves, from consideration. Nonhydrostatic modeling of an entire basin is possible, but resolution demands are extreme (see the rightmost column in Table 1 of Ref. [13]). Layered models based on the classical shallow water equations have no way to remove energy at the smallest scales (i.e., they are derived from the inviscid Euler equations), so various modifications must be made in order to faithfully represent physical phenomena on small scales. In classical hydraulics, the analogy between the shallow water equations and the equations of gas dynamics is often exploited, with the nonlinear hyperbolic theory of shocks providing a means to locally dissipate energy. On the lake scale, it is finite-wavelength dispersion that is more important to represent. One common method of simulating this phenomenon is to employ a weakly nonhydrostatic correction to the pressure [14–17]. This allows for a balance between nonlinear and dispersive terms that is otherwise impossible in shallow water theory and allows for the development of coherent wave trains, including Kelvin waves in circular domains under the  $f$ -plane approximation. Regardless of the detailed methodology, numerical modeling of lake-scale motions requires both parametrizations of physical processes (e.g., energy input from wind) and compromises on physical representation of unresolved scales (e.g., eddy viscosity).

Laboratory experiments provide an alternative means to gain information about internal seiches, though at Reynolds numbers that are considerably lower than those in the field. In a laboratory setting, a seiche can be generated by stably stratifying a long and narrow tank of water and adiabatically tilting it to some angle. Once any transient wave motion has ceased, the tank can be quickly returned to its original position and a realization of a tilted density interface is created. Since there is no force to balance buoyancy, the density interface begins to oscillate. The energy injected into the system by this action allows for relatively easy manipulation of the seiche amplitude and hence access to portions of parameter space in which large-scale oscillations coexist with smaller scale features such as shear instabilities.

A series of experiments using the methodology described in the previous paragraph were carried out by Horn *et al.* [18] in order to attempt to quantify different mechanisms responsible for the degeneration of large-scale interfacial gravity waves in lakes under the influence of different amounts of wind stress. In practice, the wind stress was parameterized through the dimensionless

amplitude,  $W^{-1} = \eta_0/h_1$  (the ratio between the initial amplitude and the upper layer depth also known as the inverse Wedderburn number [15,18–20]), of the initial basin-scale wave. The authors employed several different methods of data collection for their experiments. They attached three wave gauges to the side of a 6-m-long tank in order to measure interface displacement and recorded photographs to visually classify different degeneration mechanisms. They performed a time-scaling analysis to determine where in parameter space different degeneration mechanisms were expected to dominate. They compared the findings to field data and found that most lakes underwent a steepening of the initial basin-scale wave and formed what they labeled “solitons.” Internal solitary waves are, in fact, not solitons in the mathematical sense [21], and the trains of solitary-like waves that form in the experiments are not expected to exhibit soliton behavior when colliding with end walls and other waves.

The timescales, determined mostly via termwise balances in linear and weakly nonlinear theories, allowed for an *ad hoc* method for determining whether or not a particular mechanism was expected to dominate the degeneration of the seiche. In reality, the asymptotic expressions used for the various estimates do not have clear upper bounds on applicability in terms of seiche amplitude. Moreover, estimates based on different modes of breakdown, e.g., wave train formation versus shear instability, may not be theoretically consistent with one another. For example, internal solitary waves are based on long-wave theory [22], while the linear theory of shear instability is based on the finite-wavelength Taylor-Goldstein equation [23]. Thus, the estimates of timescales for the different mechanisms can really only be used in a small number of circumstances.

The data from the above study was analyzed further in Horn *et al.* [19] and Boegman *et al.* [20]. Horn *et al.* [19] derived a weakly nonlinear model of the interactions that solitary waves undergo in a closed basin. Where the initial assumption usually made is one of unidirectional propagating waves, Horn *et al.* [19] instead developed their model by allowing for bidirectional propagation for the subset of the cases in Horn *et al.* [18] with  $0.15 < \eta_0/h_2 < 0.6$  (the bottom layer  $h_2$  was used here because Horn *et al.* [19] instead chose to test their model against waves of elevation rather than waves of depression). Their model qualitatively agreed with the data from Horn *et al.* [18]. In Boegman *et al.* [20], the authors used the data from wave gauges to determine how the initial nonlinearity of the wave determined how energy was cascaded to small wavelengths through the emergence of a nonlinear surge. The surge serves as one possible link between large-scale oscillations, small-scale features, and wave propagation. The authors quantified the temporal distribution of available potential energy in different component horizontal wave modes and determined that the proportion of available potential energy brought to smaller scales by the nonlinear surge scaled with the nondimensional grouping  $\alpha\eta_0/c_0$ , where  $\alpha$  is the nonlinearity coefficient in the Korteweg–de Vries (KdV) equation [22,24,25],  $c_0$  is the wave speed, and  $\eta_0$  is the initial amplitude of the wave. It is worth noting that scalings based on the KdV equation also typically make the two-layer stratification assumption, since it is only in this case that closed-form expressions for the propagation speed, nonlinearity, and dispersion coefficients are available.

In this paper, high-resolution numerical simulations of the evolution of large-amplitude internal standing waves are discussed. The simulations are performed at the laboratory scale, but the length of the tank is systematically increased (decreasing the aspect ratio) since the disparity between laboratory dimensions and field scales is large. The primary goals are (i) to present detailed examples of large-amplitude wave train formation hitherto unavailable in the literature, (ii) to quantify the budget of energy in different horizontal component modes as large-amplitude seiches evolve in different combinations of aspect ratio and dimensionless amplitude, and (iii) quantify the fluid mixing as the aspect ratio and dimensionless amplitude are varied, focusing on cases where shear instabilities and wave trains coexist. The remainder of the paper is organized as follows. The methods section outlines the governing equations, as well as the numerical and analysis methods used. The results section first outlines how the breakdown into nonlinear, dispersive wave trains and shear instability varies as the aspect ratio of the tank and the location of the interface between lighter and denser fluid are varied. In particular, examples of cases where the two phenomena coexist are highlighted. A quantitative accounting for the mode-by-mode evolution of the kinetic energy of

the system is presented, as well as a semianalytical model of the evolution of the fundamental mode. Finally, using a well-known methodology from the literature, the mixing of fluid during the evolution of the seiche is characterized, illustrating a fundamental transition that occurs as the aspect ratio is decreased. The final section provides a discussion of the results and conclusions as well as suggestions for future work.

## II. METHODS

### A. Governing equations and numerical methods

Simulations are performed using the (psuedo)–spectral parallel incompressible Navier-Stokes solver (SPINS) [26]. The equations of motion that are solved are the incompressible Navier-Stokes equations under the Boussinesq approximation which are stated below:

$$\frac{\partial \mathbf{u}}{\partial t} + \mathbf{u} \cdot \nabla \mathbf{u} = -\frac{\nabla p}{\rho_0} - \frac{\rho}{\rho_0} g \mathbf{k} + \nu \nabla^2 \mathbf{u}, \quad (1)$$

$$\frac{\partial \rho}{\partial t} + \mathbf{u} \cdot \nabla \rho = \kappa \nabla^2 \rho, \quad (2)$$

$$\nabla \cdot \mathbf{u} = 0. \quad (3)$$

The unit vectors  $\mathbf{i}$  and  $\mathbf{k}$  are the unit vectors in the horizontal and positive upward directions, respectively.  $\nu$  is the kinematic viscosity,  $g$  is the gravitational acceleration,  $\rho_0$  is the reference density in the Boussinesq approximation, and  $\rho(x, z, t)$  is the density anomaly. Finally,  $\mathbf{u} = [u(x, z, t), w(x, z, t)]$  is the velocity field and  $p = p(x, z, t)$  is the pressure field. All of the cases are run on a uniform grid with, no normal flow [Eqs. (4) and (5)], and free-slip boundary conditions [Eqs. (6) and (7)]. The normal derivatives of the density field are specified at the boundary for computational purposes [Eqs. (8) and (9)]. By specifying the normal derivatives along the boundary, a cosine transform can be used to calculate the derivatives of the density field. These are described mathematically as

$$u(0, z) = u(L, z) = 0, \quad (4)$$

$$w(x, 0) = w(x, H) = 0, \quad (5)$$

$$u_z(x, 0) = u_z(x, H) = 0, \quad (6)$$

$$w_x(0, z) = w_x(L, z) = 0, \quad (7)$$

$$\rho_x(0, z) = \rho_x(L, z) = 0, \quad (8)$$

$$\rho_z(x, 0) = \rho_z(x, H) = 0. \quad (9)$$

The numerical scheme employed uses third-order Adams-Bashforth time stepping with a dynamically varying time step, and spatial derivatives are computed spectrally. The model has been thoroughly validated on a wide range of test cases [26] and has been used in many other studies [27–32], and the present simulations have been validated against past results on Kelvin-Helmholtz billows in a parallel shear flow. A grid-halving study was performed, and it was determined that the present resolution is adequate for the results presented in this paper.

The timescaling is determined through estimates for the period of oscillation from a numerical solution of the Taylor-Goldstein equation for the stratification at hand. Two-layer theory and weakly nonlinear theory based on the KdV equation both give results within a few percent and thus the scaling for period is not unique. Finally, the horizontal lengths are nondimensionalized by  $L$  (the length of the domain) and vertical lengths by  $H$  (vertical extent of the domain).

The initial condition is taken to be a quiescent fluid with a density perturbation, given mathematically as

$$\rho(x, z) = \rho_0 + \frac{1}{2}(\rho_1 - \rho_2) \tanh\left(\frac{z - [z_0 + \eta(x)]}{h}\right), \quad (10)$$

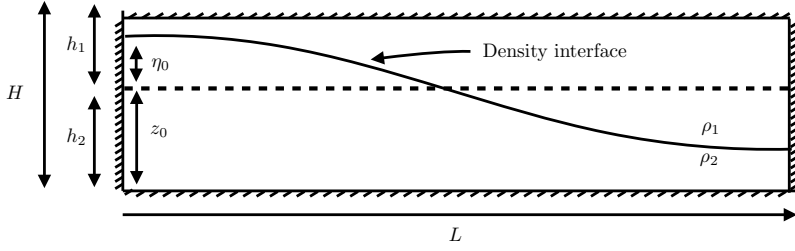


FIG. 1. Schematic of the initial condition indicating each of the layer depths ( $h_1$  and  $h_2$ ), the total depth ( $H$ ), the length ( $L$ ), amplitude ( $\eta_0$ ), and pycnocline mean depth ( $z_0$ ). The density interface is drawn as a single curve. Here,  $h_1$  and  $h_2$  are the mean upper and lower depths of the fluid.

where  $\eta = \eta_0 \cos(\frac{\pi x}{L})$  and  $\mathbf{u}(x, z, 0) = 0$ . A schematic of the initial condition is given in Fig. 1.

The relevant parameters used are  $h$  for the pycnocline half-width and the amplitude of the displacement of the density surface,  $\eta_0$ , with respect to the average depth of the pycnocline,  $z_0$ .  $z = 0$  is at the bottom, while  $z = H$  is at the top of the domain shown in Fig. 1.  $z_0$  is the distance from the domain bottom to the mean depth of the density interface.

Parameters that change across trials are in Table I and parameters that do not change are in Table II. The initial condition is chosen for mathematical simplicity and to facilitate a modal breakdown of energetics. As such, it only approximately represents the state that the density interface would take in a tilted-tank experiment. Numerical experiments have been performed on a version of the linear interface and the qualitative agreement with the results below was excellent. Quantitative differences will be described in a separate publication. Indeed, in a lake, the interface

TABLE I. Table containing all cases considered in this paper. Cases are characterized by depth above middepth in mm (e.g., a prefix of 15 means that the average depth of the pycnocline is 15 mm above  $H/2$ ), amplitude with  $Q < P < L$  (smallest to largest), the pycnocline half-width in mm, and finally tank length specified after the underscore (1m is a tank length of 1 meter, etc.).

Case	$N_x \times N_z$	$z_0$ (m)	$\eta_0$ (m)	$L$ (m)	$\eta_0/h_1$	$H/L$
Q5-1m	$2048 \times 512$	0.125	0.05	1	0.4	0.25
P5-1m	$2048 \times 512$	0.125	0.065	1	0.52	0.25
L5-1m	$2048 \times 512$	0.125	0.0825	1	0.66	0.25
15L5-1m	$2048 \times 512$	0.14	0.0825	1	0.75	0.25
25L5-1m	$2048 \times 512$	0.15	0.0825	1	0.825	0.25
Q5-2m	$4096 \times 512$	0.125	0.05	2	0.4	0.125
P5-2m	$4096 \times 512$	0.125	0.065	2	0.52	0.125
L5-2m	$4096 \times 512$	0.125	0.0825	2	0.66	0.125
15L5-2m	$4096 \times 512$	0.14	0.0825	2	0.75	0.125
25L5-2m	$4096 \times 512$	0.15	0.0825	2	0.825	0.125
Q5-4m	$8192 \times 512$	0.125	0.05	4	0.4	0.0625
P5-4m	$8192 \times 512$	0.125	0.065	4	0.52	0.0625
L5-4m	$8192 \times 512$	0.125	0.0825	4	0.66	0.0625
15L5-4m	$8192 \times 512$	0.14	0.0825	4	0.75	0.0625
25L5-4m	$8192 \times 512$	0.15	0.0825	4	0.825	0.0625
Q5-8m	$16384 \times 512$	0.125	0.05	8	0.4	0.03125
P5-8m	$16384 \times 512$	0.125	0.065	8	0.52	0.03125
L5-8m	$16384 \times 512$	0.125	0.0825	8	0.66	0.03125
15L5-8m	$16384 \times 512$	0.14	0.0825	8	0.75	0.03125
25L5-8m	$16384 \times 512$	0.15	0.0825	8	0.825	0.03125

TABLE II. Unchanged physical parameters for the cases in Table I.  $\nu$  is the kinematic viscosity,  $\kappa$  is the coefficient of heat diffusion, Sc is the Schmidt number (the ratio of kinematic viscosity to diffusivity),  $h$  is the half-width of the pycnocline,  $\Delta\rho$  is the density difference between upper and lower layers as a percentage of the total density difference,  $\rho_0$  is the constant density of the fluid, and  $H$  is the total depth.

$\nu$ (m <sup>2</sup> /s)	$\kappa$ (m <sup>2</sup> /s)	Sc	$h$ (m)	$\Delta\rho$	$\rho_0$ (kg/m <sup>3</sup> )	$H$ (m)
$1 \times 10^{-6}$	$1.4 \times 10^{-7}$	7	0.005	0.02	1000	0.25

shape can be much more complicated than a linear tilt. This is due to spatiotemporal variations in wind forcing and influences of bottom topography and lake shape. For example, Fig. 3 of Henderson and Deemer [10] shows temperature measurements from an acoustic Doppler profiler in Lacmas Lake in Washington state, USA. It can clearly be seen in their figure that the different isotherms do not have the same angle of tilt with respect to the surface.

Several different dimensionless numbers are typically used to characterize the setup. In the nonlinear internal wave literature, the Reynolds number is often estimated as

$$\text{Re} = \frac{cH}{\nu},$$

where  $c$  is an estimate of the internal wave speed,  $H$  is the total depth, and  $\nu$  is the kinematic viscosity. For a typical laboratory setup,  $\text{Re} \approx 4 \times 10^4$ , while for a typical lake,  $\text{Re} \approx 4 \times 10^7$ . While this is a sizable disparity, in both cases viscous effects are essentially negligible. This statement would need to be revisited in a detailed consideration of boundary layer effects, something we do not pursue in the present paper. A second dimensionless parameter is the aspect ratio,

$$\mu = \frac{H}{L}.$$

For laboratory scales,  $\mu$  varies over the range  $0.03 < \mu < 0.25$  while in the field much smaller values are typical, with  $\mu \approx 0.004$  being a reasonable estimate for midsized lakes. The scaled amplitude of the seiche provides a third dimensionless parameter, following the convention in Horn *et al.* [18]. We refer to this as the inverse Wedderburn number, defined as

$$W^{-1} = \frac{\eta_0}{h_1}.$$

These choices are consistent, albeit using somewhat different notation, with the theory of weakly nonlinear internal waves as expressed in the KdV equation [33]. Weakly nonlinear theory performs an asymptotic expansion in  $W^{-1}$  and  $\mu$ , and hence organizing results by these two parameters allows for our simulations to meaningfully connect with KdV theory. An alternative formulation would define the Froude number as the ratio between a characteristic velocity and a characteristic wave speed and use it to characterize instances of wave breaking or instability onset. This was done in Horn *et al.* [18] along with a discussion of the gradient Richardson number, which is used to characterize the possibility of linear instability of stratified, parallel shear flows. Both of these rely on *a priori* estimates of velocity, which are not natural in the setting of the adjustment problem. A final dimensionless parameter is Sc, the Schmidt number, defined as the ratio of kinematic viscosity to diffusivity. For all simulations presented in this paper, this value is held constant at  $\text{Sc} = 7$ , the value relevant for temperature-stratified fluids.

## B. Energetics

The oscillation of the seiche is due to a transfer of available potential energy to kinetic energy and back through the buoyancy flux [34]. These two quantities are defined and discussed below.

### 1. Potential energy

In the field analog to the following numerical experiments, the stress on the surface due to the wind provides an initial input of potential energy. The potential energy density,  $E_p$ , of a fluid is defined as the following:

$$E_p = \frac{1}{HL} \int_0^L \int_0^H \rho(x, z, t) g z dz dx, \quad (11)$$

where  $\rho(x, z, t)$  is the full density field. Here, the integral in the  $y$  direction is taken to be 1 because all cases are two dimensional and the density field is independent of that dimension. With the continuously stratified model, the available potential energy density,  $E_a$ , can be calculated. The  $E_a$  is the fraction of the total  $E_p$  available to be converted to kinetic energy, KE. This quantity is calculated over time by simply performing the following operation:

$$E_a = \frac{1}{HL} \int_0^L \int_0^H [\rho(x, z, t) - \tilde{\rho}(z, t)] g z dz dx. \quad (12)$$

$\tilde{\rho}(z, t)$  is the adiabatically rearranged density field. The above equation brings about the notion of the background potential energy, or  $E_b$ . The  $E_b$  is the potential energy of the fluid if it were motionless and adiabatically rearranged to its stable state. Calculating the  $E_b$  can be a computationally expensive process due to the determination of the stably stratified density field at every step and may be hard to define in an open system. Since the systems that are considered in this paper are all closed, this is not a problem. In this paper, the  $E_b$  is given by

$$E_b = \frac{1}{HL} \int_0^L \int_0^H \tilde{\rho}(z, t) g z dz dx. \quad (13)$$

Thus, the concept of  $E_a$  in continuously stratified fluid is

$$E_a = E_p - E_b. \quad (14)$$

Using the continuous representation of the  $E_a$ , a two-layer approximation can be created denoted by  $E_a^{(2)}$ . Using this model of the  $E_a$ , useful insights on how the  $E_a$  redistributes within the wave field can be gained. The formula is derived by assuming an infinitely thin interface and making the rigid lid approximation. In order to do this numerically, the average depth of the pycnocline is calculated at every time output. The method removes any sort of wave breaking and instabilities (convective or shear) that may occur and thus truly represents an approximation of the  $E_a$ . The equation for  $E_a^{(2)}$  is given by

$$E_a^{(2)} = \frac{1}{2} \frac{g \Delta \rho \rho_0}{HL} \int_0^L \eta^2(x) dx. \quad (15)$$

Note here that since the simulations are two dimensional, the units of  $\rho_0$  are  $\text{kg/m}^2$  and  $\Delta \rho$  is unitless. These ensure that  $E_a^{(2)}$  has the correct dimensions. In the experimental studies by Horn *et al.* [18] and Boegman *et al.* [20], the primary method of analysis relies on the two-layer approximation when characterizing various regimes of degeneration. In this paper, the two-layer representation of the  $E_a$  is used to build a model of the rate of energy extraction from the fundamental mode of the seiche. This model is built by using spectral analysis to partition potential energy into different harmonics using Parseval's theorem [35]. Thus, insight on the motion can be gained by considering only the interface displacement and not the entire continuously stratified fluid. The boundary conditions for the density field in a continuously stratified fluid [Eqs. (8) and (9)] give the two layer analog of  $\frac{\partial \eta}{\partial x} \Big|_{x=0,L} = 0$ . This implies that  $\eta$  can be written in the following way:

$$\eta = \sum_{n=1}^{\infty} \hat{\eta}_n \cos(k_n x), \quad (16)$$

with wave number  $k_n = \frac{n\pi}{L}$  and expansion coefficient  $\hat{\eta}_n$ . By replacing  $\eta^2(x)$  in Eq. (15) with the cosine series in Eq. (16) and simplifying the integral, the two-layer representation of the  $E_a$  in Fourier space is

$$E_a^{(2)} = \frac{1}{4} \frac{g \Delta \rho \rho_0}{H} \sum_{n=1}^{\infty} \hat{\eta}_n^2. \quad (17)$$

Now, individual harmonics can be discussed with respect to the  $E_a$ . In the numerical simulations presented in this paper, the harmonic number is bounded above by the number of grid points in the horizontal direction.

## 2. Kinetic energy

The kinetic energy, or more simply KE, in two dimensions with velocities homogeneous in the  $y$  direction with no rotation in a Boussinesq fluid is given by

$$\varphi_k = \frac{1}{2} \rho_0 [u(x, z, t)^2 + w(x, z, t)^2]. \quad (18)$$

The vertical mean of the KE is computed simply by integrating the above equation vertically,

$$E_k^{(p)} = \frac{1}{H} \int_0^H \frac{1}{2} \rho_0 [u(x, z, t)^2 + w(x, z, t)^2] dz. \quad (19)$$

The above description of the kinetic energy allows for the retention of horizontal and temporal information while making the data easier to interpret. Alternatively, at the expense of spatial information, information about the wave-number spectrum can be gained by transforming the above quantity into wave-number space. This operation begins from the stream function representation of the flow field,

$$\psi(x, z, t) = \sum_{n=1}^{\infty} a_n \sin(k_n x) \phi_n, \quad (20)$$

from which the velocity field components are computed as  $u = \psi_z$ , and  $w = -\psi_x$  so that

$$u = \sum_{n=1}^{\infty} a_n \sin(k_n x) \phi_n'(z),$$

$$w = - \sum_{n=1}^{\infty} a_n k_n \cos(k_n x) \phi_n(z).$$

To compute the KE,  $u$  and  $w$  are squared, summed together, and horizontally averaged over the entire domain. Orthogonality allows for the simplification

$$\frac{1}{2} \rho_0 \int_0^L u^2 + w^2 dx = \frac{1}{2} \rho_0 \sum_{n=1}^{\infty} [a_n^2 (\phi_n')^2 + (a_n k_n)^2 (\phi_n)^2], \quad (21)$$

where the  $z$  dependence of the vertical structure function and its derivative has been suppressed. To tidy up the notation, the following notation is introduced:

$$\hat{u}_n^2 = a_n^2 (\phi_n')^2, \quad (22)$$

$$\hat{w}_n^2 = (a_n k_n)^2 (\phi_n)^2, \quad (23)$$

and vertically averaging Eq. (21) then gives

$$E_k^{(f)} = \frac{1}{2} \frac{1}{H} \int_0^H \frac{1}{2} \rho_0 \sum_{n=1}^{\infty} (\hat{u}_n^2 + \hat{w}_n^2) dz. \quad (24)$$

This representation of the kinetic energy is a function of wave number and time as the fluid evolves.

The rate of change of the total pseudoenergy, kinetic plus available potential, in a continuously stratified fluid can be written as [34]

$$\frac{d}{dt}(\text{KE} + E_a) = -\epsilon - \varphi, \quad (25)$$

where  $-\epsilon$  represents the volume integrated losses due to momentum diffusion and  $-\varphi$  represents the volume integrated losses due to fluid mixing. Using Eqs. (19) [or equivalently (24)] and (12), the total pseudoenergy is seen to decrease slowly due to viscous dissipation and mixing. For small-amplitude seiches, it is conserved essentially exactly and in the most vigorous cases roughly 10% of the initial pseudoenergy is lost to viscous dissipation and mixing over two periods. The two-layer approximation of the  $E_a$  is used only as an *a posteriori* diagnostic and to build a semiquantitative model of seiche decay rate.

### C. Mixing characterization

There are different ways in which mixing of fluid layers can be quantified. Energetically speaking, irreversible mixing of a fluid can be characterized by an increase in the  $E_b$  [34,36]. This process makes potential energy inaccessible for oscillation and thus results in damping of the fluid motion. This characterization of mixing is quantified by the energetic mixing characterization and is referred to as  $M_E$ :

$$M_E = \frac{1}{E_b(0)} \frac{1}{HL} \int_0^L \int_0^H \tilde{\rho}(z, t) g z dz dx - 1, \quad (26)$$

where  $\tilde{\rho}(z, t)$  is the adiabatically rearranged density field in Eq. (12).

Finally, the analysis below is based on making an approximation that the flow is independent of variation in the spanwise ( $y$ ) direction. This is a reasonable assumption if the spanwise dimension of a tank in a laboratory for an analogous three-dimensional experiment is not large with respect to the length. The dominant dynamics will then be approximately independent of the spanwise dimension. Since all the simulations described below are two dimensional, missing are some important mechanisms such as the vortex tilting and stretching mechanisms. These are known to contribute to three-dimensional effects in the fluid flow and are unable to occur in two dimensions [23]. However, in some circumstances, the coastal oceanography of fjords being an example, it is reasonable to restrict analysis to two dimensions. As mentioned earlier, Horn *et al.* [18] used tank dimensions (in units of meters) of  $(X, Y, Z) = (6.00, 0.30, 0.29)$  and Lamb and Nguyen [37] used a two-dimensional, fully nonlinear, nonhydrostatic numerical model for calculating the energy flux of an internal solitary wave reflecting off of a boundary. In both of these examples, dynamics studied were all on length scales relevant to a laboratory.

As an aside, a local measure of scalar mixing can be defined in different ways. One could take the approach of Ref. [38], where the scalar mixing is proportional to the time rate of change of the square magnitude of the gradient of the scalar (e.g., the density field). A second possibility is to use the sorted density field to define a background density and through this an available potential energy [34]. Irreversible mixing has been characterized using this technique in a number of references, for example, Refs. [37,39,40].

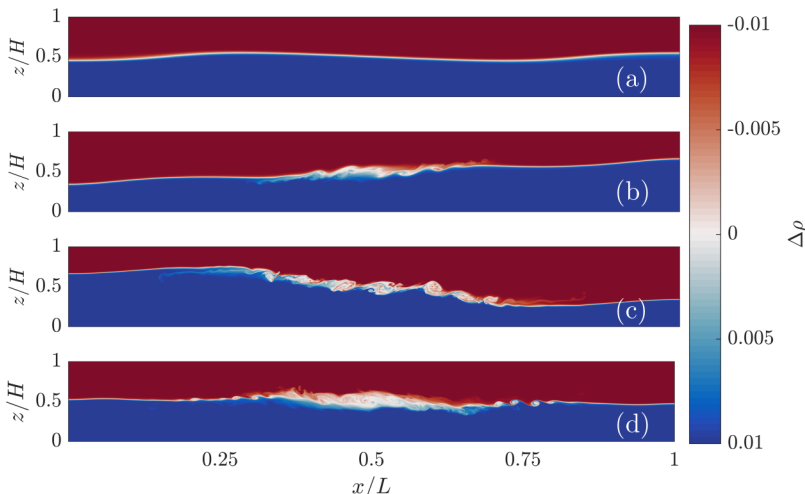


FIG. 2. Snapshots of the density field, with the interface particularly prominent, for the L5-2m case. Density fields taken at  $\tau = 0.25, 0.7, 0.9,$  and  $1.25$ .

### III. RESULTS

The results section is broken up into six subsections. First, the evolution of the symmetric cases where  $h_1 = h_2 = 0.5H$  is discussed at several representative domain lengths (and hence aspect ratios). The first is  $L = 2\text{ m}$  (L5-2m) followed by  $L = 8\text{ m}$  (L5-8m). The reason these lengths are chosen is that they show two different mechanisms responsible for the degeneration of the seiche. Next, the quantitative breakdown of the energy into harmonics for these cases is discussed. Following the discussion of the symmetric cases is a discussion of the skew cases (15L5-8m and 25L5-8m), where  $h_1 \neq h_2$ . Again, this is followed by a detailed mode breakdown of the energy. Following the analysis of the skew cases is a discussion of the KE and the  $E_a$  of several cases compared to one another. This section concludes with a discussion of irreversible mixing. The results in the following section are presented using perceptually uniform color maps as to avoid instances of artificial gradients [41].

#### A. Symmetric cases: Qualitative aspects of evolution

First consider the L5-2m and L5-8m cases, both with equal layer depths. In Figs. 2 and 3, the density interface at different nondimensional times is plotted to qualitatively compare the flow evolution. In particular, the differences in the shape of the density interface as the tank length is changed is of particular interest here.

Consider first Fig. 2, which shows the temporal evolution of the L5-2m case. The first panel, (a) is at  $\tau = 0.25$ , (b) is at  $\tau = 0.7$ , (c) is at  $\tau = 0.9$ , and (d) is at  $\tau = 1.25$ . At early times, the density interface is stable and there are two small-amplitude waves steepening on either side of the node propagating inward from the sidewalls. As time moves forward, shear instabilities form on the density interface as the wave oscillates. At later times, the shear instabilities have completely collapsed, the pycnocline has noticeably widened, and there is evidence of a secondary shear instability event. The instabilities in this case form at the node of the wave. This is not unlike the results from Thorpe [42], who showed that there is vortex motion created at the node which induces overturning (see their Fig. 14).

Next, when comparing L5-2m to the longer case L5-8m, there are some similarities at early times, but fundamental differences at later times. The snapshots are taken at the same nondimensional times. Early in the evolution, the density interface is qualitatively similar to that of the L5-2m case,

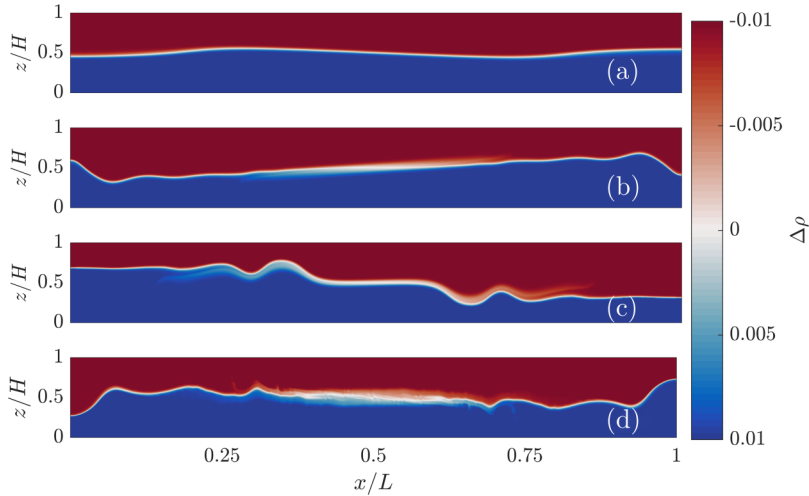


FIG. 3. Snapshots of the density field, with the interface particularly prominent, for the L5-8m cases. Density fields taken at  $\tau = 0.25, 0.7, 0.9,$  and  $1.25$ .

but instead of the shear instabilities seen in Fig. 2, the generation of higher harmonics takes place. The evolution appears to begin with two counterpropagating waves originating from the left and right walls propagating inward. They interact at the node and then continue to propagate outward toward the opposite wall from where they originated with only a small amount of disruption at the node.

Comparing Figs. 2 and 3, it is clear that the mode of degeneration is fundamentally different when the length of the tank is increased. It appears that in the shorter cases (including L5-1m, which was not shown), shear instabilities dominate the dynamics, while in the longer cases (including L5-4m, not shown), the seiche develops into higher harmonics and coexists with smaller scale instabilities.

In Figs. 4 and 5, the vorticity field and KE field are shown for the L5-2m and the L5-8m cases at  $\tau = 0.9$ . In Fig. 4, the black lines denote two characteristic isopycnals, and in Fig. 5, the white lines serve the same purpose. These figures serve to show that the vorticity at this time is mostly

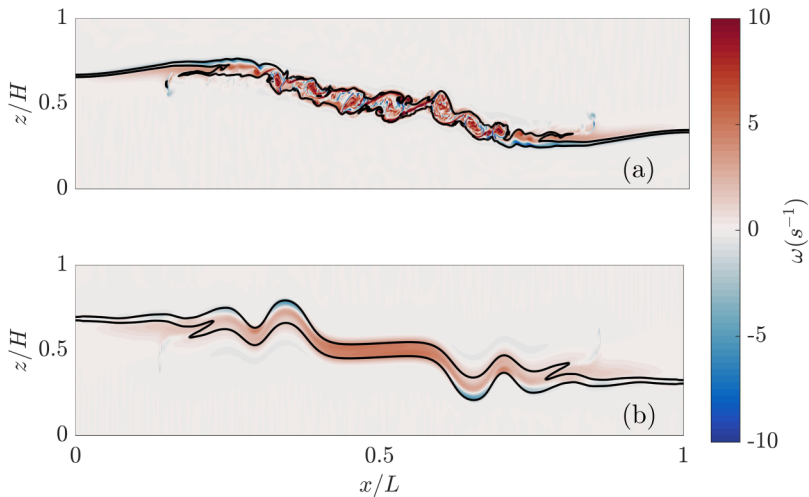


FIG. 4. The vorticity field for the L5-2m (top) and L5-8m (bottom) cases at  $\tau = 0.9$ .

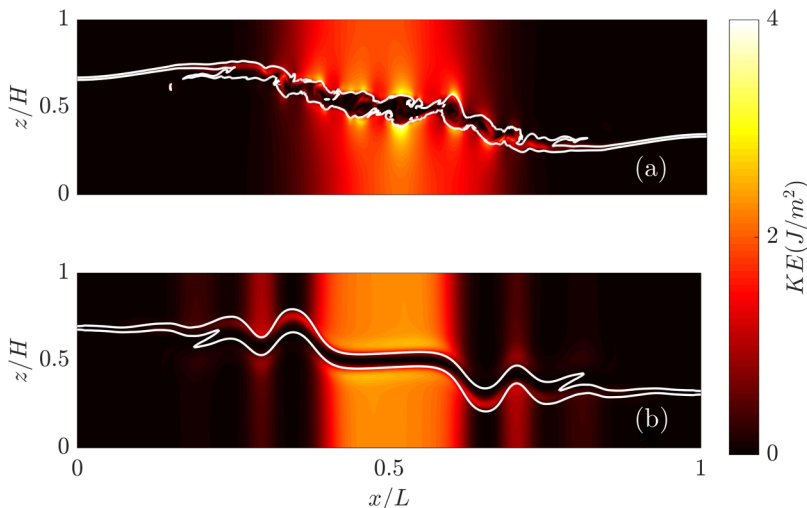


FIG. 5. The KE field for the L5-2m (top) and L5-8m (bottom) cases at  $\tau = 0.9$ .

induced by the oscillation of the wave, but there are small patches of vorticity induced in the opposite direction. The shorter case, which shows signs of vigorous shear instability, contains many high gradients of vorticity, while the longer case, which has a more stable pycnocline, has few high gradients. This is, of course, due to the formation of high-density gradients in the L5-2m case, which induces rotation of fluid particles and the apparent lack thereof in the L5-8m case. The KE fields show that the spatial distribution of KE in the shorter of the two cases considered is mostly near the node at this time, while in the longer of the two cases, some is transferred around the domain due to the formation of the waves.

### B. Symmetric cases: Quantitative analysis of degeneration

Figures 6(a) and 6(c) show the vertically averaged KE of the L5-2m and L5-8m cases, respectively, as a function of time and space. Along the vertical axis is nondimensional time, and along the horizontal axis is the horizontal dimension normalized by the length of the tank,  $x/L$ . Figures 6(b) and 6(d) show a basic breakdown of the power spectral density [35] for the L5-2m case and L5-8m cases respectively. The green line is the total KE density normalized by its maximum value over the first two seiche periods, the red line represents the normalized KE in the first four harmonics, and the blue line represents the normalized KE in every other harmonic for each case.

The horizontal distribution of the KE is apparent as both Figs. 6(a) and 6(c) show how it is broken up into lobes. Where these two differ is that the KE in the longer of the two cases [Fig. 6(c)] is redistributed into many higher harmonics, while the KE of the shorter of the two cases appears to maintain a consistent distribution across the entire tank. There are also Kelvin-Helmholtz billows, denoted by stationary vertical streaks, in this case, whereas there are not in the longer case. The redistribution of energy is apparent in the PSD of each of these cases. For the shorter case [Fig. 6(b)], the KE in the lowest harmonics is almost the same as the KE of all of the harmonics, while in the longer case [Fig. 6(d)], there is a clear difference in how the higher harmonics are activated.

### C. Skew cases: Qualitative aspects of evolution

The following section outlines the qualitative evolution of a case where the layer depths are no longer equal, meaning that  $z_0$  has been changed. Snapshots of the 15L5-8m case are shown in Fig. 7. By introducing the asymmetry between the layer depths, different kinds of motion are expected. A

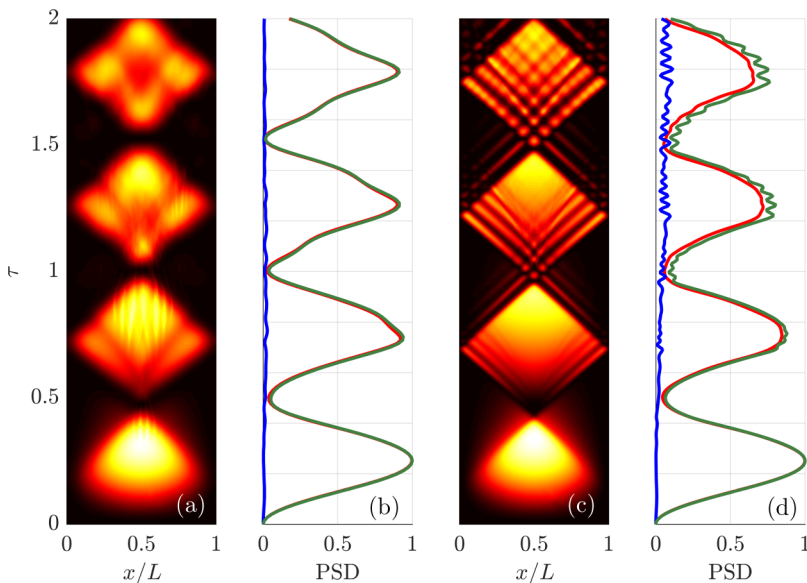


FIG. 6. [(a), (c)] Space-time plot for the vertically integrated KE normalized by the maximum for the L5-2m and L5-8m cases, respectively. [(b), (d)] Green line represents the total KE normalized by the maximum. The red line represents the energy stored in the first four harmonics, and the blue line represents the rest of the energy for each case.

primary finding of weakly nonlinear theory (WNL) is that when the layer depths of a stratified fluid are unequal, nonlinear steepening is expected to occur. In the limit of a two-layer stratification with an infinitesimally thin interface separating the two layers, the rate at which steepening is expected to occur is given by [22,24,25]

$$\alpha = \frac{3c_0}{2} \frac{(h_1 - h_2)}{h_1 h_2}. \quad (27)$$

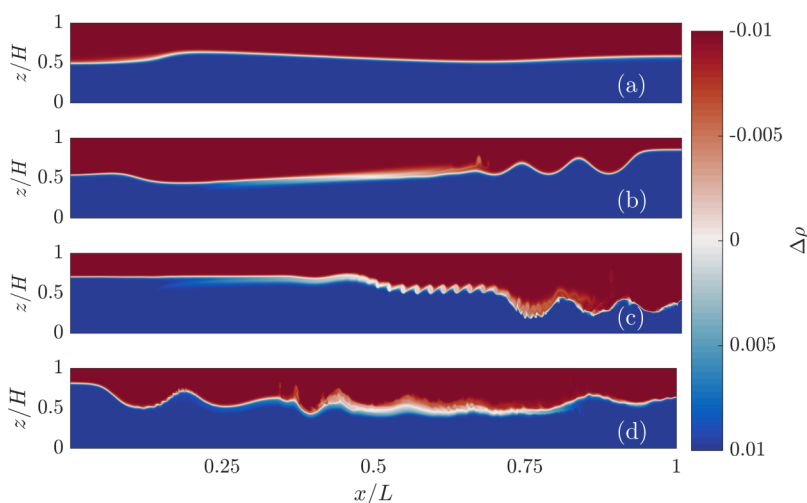


FIG. 7. Snapshots of the density field, with the interface particularly prominent, for the 15L5-8m case. Density fields taken at  $\tau = 0.25, 0.7, 0.9,$  and  $1.25$ .

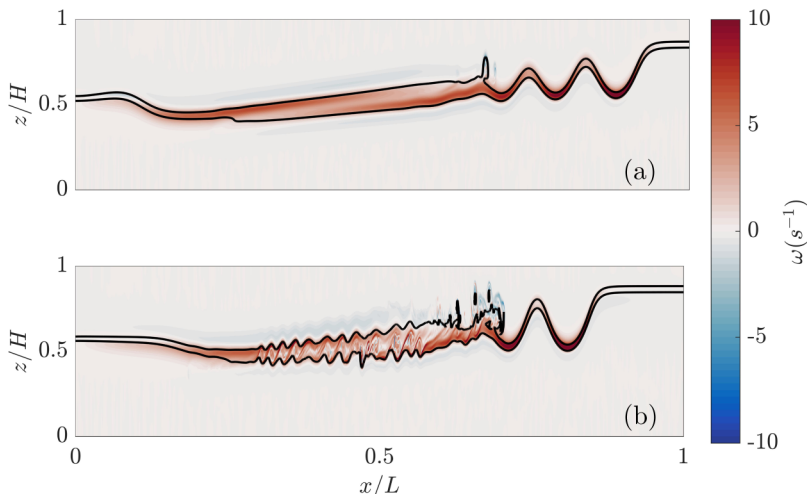


FIG. 8. The vorticity field for the 15L5-8m (top) and 25L5-8m (bottom) cases at  $\tau = 0.7$ .

Here,  $h_1 = H - z_0$  and  $h_2 = z_0$ . Clearly, the rate of nonlinear steepening is proportional to the disparity in layer depths, meaning that if these values are different, steepening should occur quickly, while if they are close to one another, steepening should occur at a slower rate.

The snapshots of the density field for the 15L5-8m case (Fig. 7) are taken at the same nondimensional times as the L5-2m and L5-8m cases. Almost immediately, a progressive surge forms on the left-hand side of the domain. This surge propagates rightward and steepens, eventually dispersing into a solitary wave train. The solitary waves propagate and trigger shear instabilities which are then smoothed out by the passing wave which is different than the cases previously discussed. A smaller effect present in both cases is the formation of shear instabilities within the trough of the leading propagating wave. This sort of instability was pointed out by Grue *et al.* [43] and studied by Barad and Fringer [44] and then by Carr *et al.* [45]. Troy and Koseff [46] showed through a series of progressive wave-breaking experiments that the emergence of Kelvin-Helmholtz instability within the wave is dependent on the ratio of timescales of the steepening of the instabilities to the wave period of the waves being considered.

In Fig. 8, the vorticity field for the 15L5-8m and 25L5-8m cases at  $\tau = 0.7$  is shown for comparison. As expected, the vorticity is confined between the characteristic isopycnals and is all positive due to the large-scale oscillation of the seiche. However, the intense positive vorticity at the peaks of the solitary waves due to their propagation across the domain. There are shear instabilities that appear in the 25L5-8m case which create high-wave-number variations in the vorticity field in the middle section of the tank, but the large-scale vorticity is very similar in character to the 15L5-8m case. The KE for these cases is qualitatively similar as well, shown in Fig. 9. Toward the right-hand side of both cases, the KE has been redistributed into higher harmonics, while it is kept as one large-scale structure to the left of the wave packet. The 15L5-8m case appears to form three vertical bands of KE to the right of the node, while the 25L5-8m case appears to form only two. As well, in the 25L5-8m case, the shear instabilities trigger to the left of the wave packet appear to distribute the energy in even smaller scales.

#### D. Skew cases: Quantitative analysis of degeneration

The vertically averaged KE for the 15L5-8m and 25L5-8m cases is shown in Fig. 10. Immediately, the symmetry seen in Fig. 6 is lost due to the formation of the surge and the resulting solitary waves. Lobes symmetric about the center of the tank are no longer formed. Instead, streaks across the domain are formed due to the formation of the propagating wave packets. The dimensionless

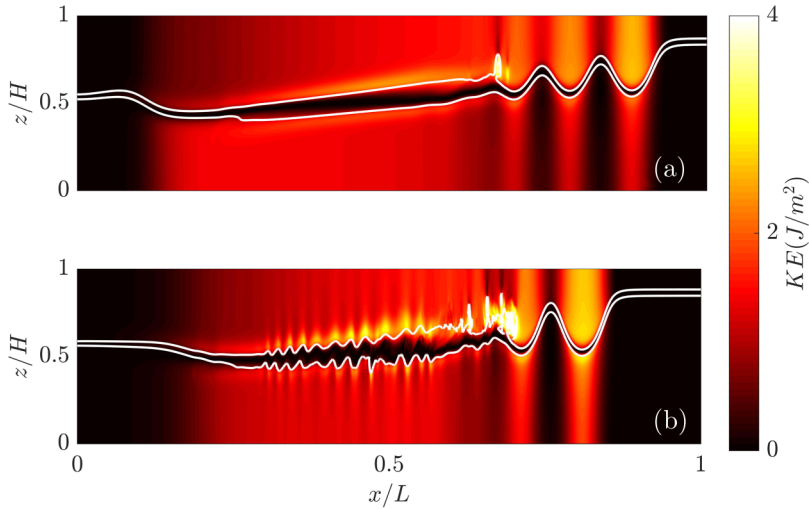


FIG. 9. The KE field for the 15L5-8m (top) and 25L5-8m (bottom) cases at  $\tau = 0.7$ .

amplitude appears to affect how many propagating waves form in these cases. This qualitatively agrees with the notion that, unlike nonlinear steepening, dispersive behavior is most prominent when the layer depths are equal. Qualitative similarities are seen the PSD for each case. The disparity between the low harmonic and total KE becomes noticeably different early on for both cases and the small-scale KE subsequently increases.

These results share similarities with the results presented in Horn *et al.* [18] and Boegman *et al.* [20]. Figure 2 in Horn *et al.* [18] shows in parameter space the dominant degeneration mechanism

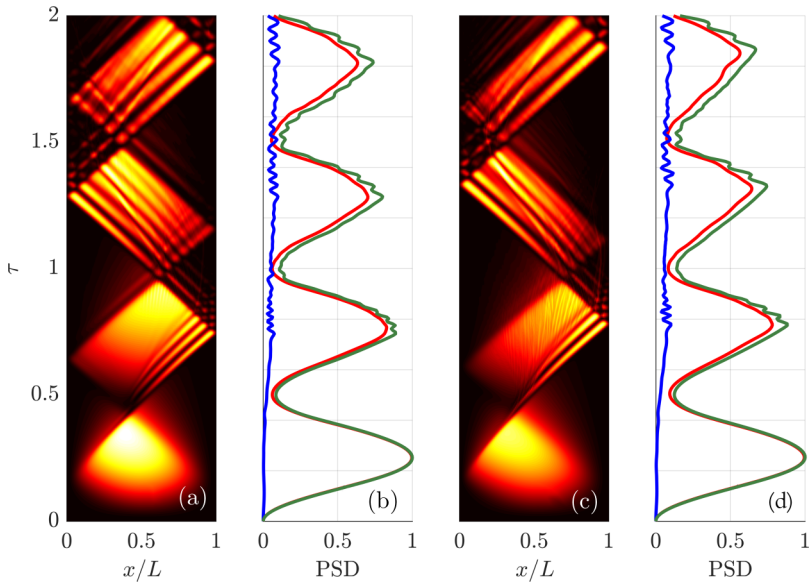


FIG. 10. [(a), (c)] Space-time plot for the vertically integrated KE normalized by the maximum for the 15L5-8m and 25L5-8m cases, respectively. [(b), (d)] Green line represents the total KE normalized by the maximum. The red line represents the energy stored in the first four harmonics, and the blue line represents the rest of the energy for each case.

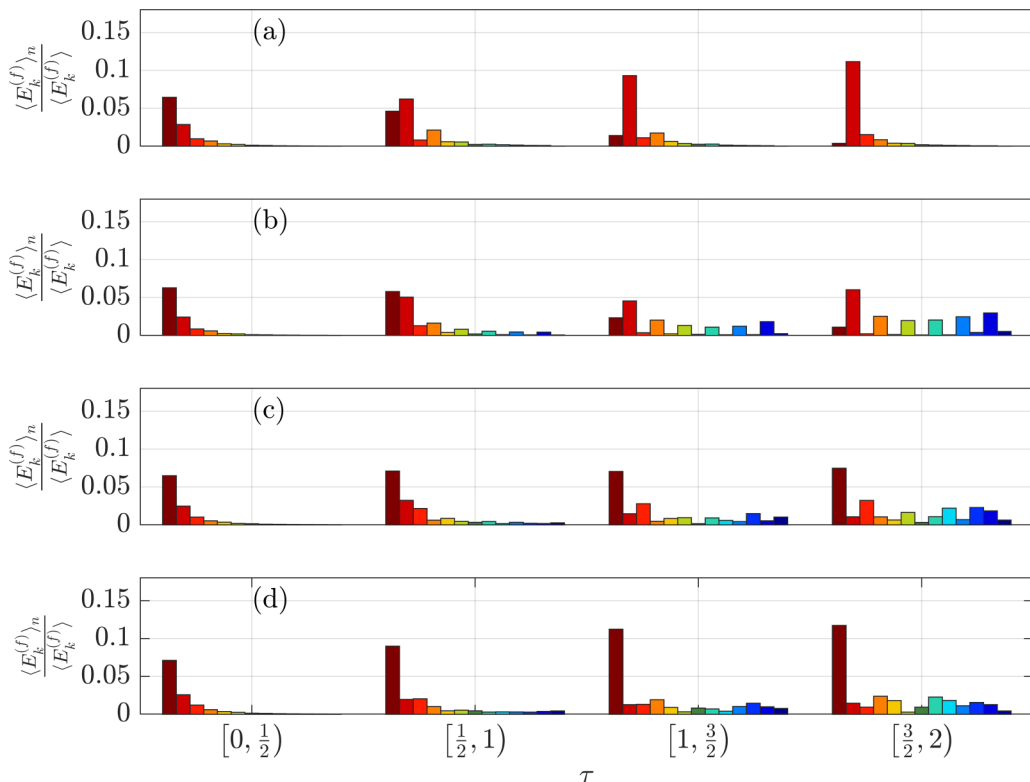


FIG. 11. The vertically averaged KE in each harmonic from modes 2 to 17. The first harmonic is ignored because it composes most of the KE and thereby skews the plots. The horizontal axis is broken down by half-period groupings. The vertical axis is normalized by the total KE for time average over each half period: (a) L5-2m, (b) L5-8m, (c) 15L5-8m, and (d) 25L5-8m.

of the seiche. Much of the parameter space is occupied by what they label as “solitons,” meaning that in most cases, solitary waves will occur and move energy around the basin. However, Figs. 2, 3, and 7 show that there is typically more than one instability that may occur over the course of the early evolution of these waves. For instance, the only case where Horn *et al.* [18] saw KH billows was the case with equal layer depths and a large initial amplitude, but clear billowing was seen in three of the four cases discussed in this paper. The aspect ratio of the tank also appears to play an important role in which degeneration appears (at least initially). The L5-2m and L5-8m cases have the same relative layer depths and initial amplitude but clearly have different dominant degeneration mechanisms. Since the results presented in this paper are numerical, the spatial representation of the KE is more readily available than the spatial features of the  $E_a$ , so an effort is made to use both KE and  $E_a$  in the following discussion in order to compare to the results of Horn *et al.* [18] and Boegman *et al.* [20].

### E. Comparison of energetics across cases

The above discussion is meant to be a qualitative analysis of a subset of representative cases. Now, a quantitative discussion can be performed describing how they relate to one another as well as other cases that were not shown above.

Figure 11 shows the KE per mode, time averaged over the first four half periods and then normalized by the maximum KE over each half period (meaning the first grouping is scaled by the maximum of the KE in the first half period of the seiche, etc.). Each grouping of bars represents

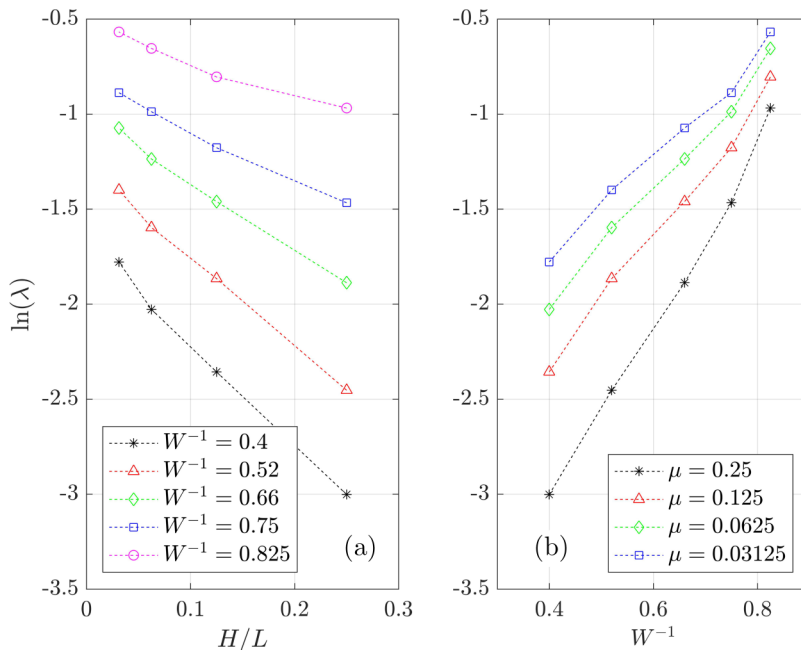


FIG. 12. The logarithm of the decay parameter  $\lambda$  calculated via linear regression of the maximums of the potential energy from the first harmonic, as a function of the dimensionless amplitude  $\eta_0/h_1$  and aspect ratio  $\mu = H/L$ .

harmonics 2 to 17 from left to right. The first harmonics for each case have been removed from the plots because they encompass the vast majority of the total KE. Figure 11(a) shows the results for L5-2m, Fig. 11(b) shows results for L5-8m, Fig. 11(c) shows those for 15L5-8m, and Fig. 11(d) shows those for 25L5-8m. Figure 11 illustrates that the way in which energy is passed to different modes differs when the dimensionless amplitude and aspect ratio are changed. At reasonably large aspect ratios, there appears to be a particular harmonic that has the most energy [the third harmonic in Fig. 11(a)] and the amount of energy decays with higher harmonics. When the aspect ratio is reduced, it appears as if certain harmonics are favored over others [third, fifth, seventh, and onward in Fig. 11(b)], changing the small-scale behavior. It is worth briefly drawing an analogy with the classical Stokes wave here [23]. The Stokes wave solution expands a finite-amplitude wave as a trigonometric series in nondimensional amplitude and wave number. A standing Stokes wave could be obtained by superimposing two counterpropagating Stokes waves. Typically, for surface waves the first three terms of the approximating series are given in the expansion of the free surface. The coefficients decrease monotonically, meaning that any nonmonotonicity in the bar graphs shown in Fig. 11 can be taken as an indication that the motion in the simulations is more complex than a Stokes wave. Upon increasing the dimensionless amplitude, the second harmonic is favored over the rest; however, there appears to be a more even distribution over the higher harmonics. Thus, the asymmetry present in the 15L5-8m and 25L5-8m cases appears to remove any bias to a certain set of harmonics that may occur if the layer depths were equal.

Because the aspect ratio and the dimensionless amplitude of the initial condition appear to affect which harmonics are excited with KE, it is of use to discuss how these changes are manifested in the spatial distribution of the  $E_a$  of the seiche. Hypothetically speaking, the contribution of every mode could be discussed, *but* more can be learned if only the lower harmonics are considered. This can help build an understanding of which modes are excited during the evolution of the seiche. The reason why the rate at which  $E_a$  is extracted from the first harmonic may be of interest is because the large-scale oscillation of the seiche effectively forms the background state that the smaller scale

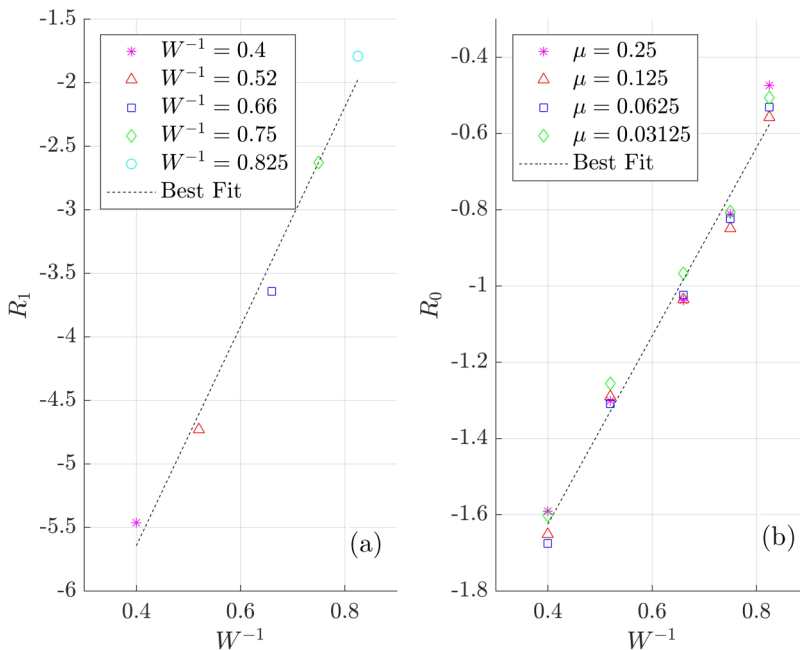


FIG. 13. Fitting parameters for the model of  $\lambda(W^{-1}, \mu)$ . Definitions are given in the text.

wave motion can extract energy from. Thus, a model for the  $E_a$  in the first harmonic is proposed as follows:

$$\tilde{E}_a^{(2)} = E_a(0)e^{-\lambda\tau} \cos^2(2\pi\tau), \quad (28)$$

where  $E_a(0)$  is the initial  $E_a$  input and  $\lambda$  is an  $E_a$  decay rate. The  $\cos^2(\cdot)$  is meant to emulate the oscillatory nature of the  $E_a$ , but can be ignored if only the net losses of  $E_a$  are of interest.  $\lambda$  is assumed to be a function of two nondimensional bulk parameters,  $W^{-1}$  and  $\mu$ , these being the dimensionless amplitude (or inverse Wedderburn number [15,18]) and the aspect ratio of the tank.  $\lambda(W^{-1}, \mu)$  gives an empirical measure for how energy is extracted from the fundamental harmonic of the seiche in  $W^{-1} - \mu$  parameter space. This could give an indication of the timescale on which the large-scale seiche degenerates into higher mode waves and how fast nonlinear effects become present in the flow.  $\lambda = \lambda(W^{-1}, \mu)$  is computed by calculating the  $E_a$  of the fundamental mode of oscillation of the seiche using  $n = 1$  in Eq. (17) and finding the maxima and the times at which they occur during the evolution of the seiche.

In Figs. 12(a) and 12(b), the rate of decay of the  $E_a$  in the first harmonic is shown. For all cases with constant  $W^{-1}$ , the decay rate of the first harmonic decreases with increasing aspect ratio. Thus,  $E_a$  is extracted from the first harmonic at a higher rate for longer initial wavelengths than for shorter. These results agree qualitatively with the plots of the density fields in Figs. 2 and 3 because of the absence of higher mode deflections of the density interface in the L5-2m and the presence of them in the L5-8m case. Physically, the breakdown of a seiche into nonlinear dispersive wave trains is

TABLE III. Dimensionless parameters which determine how  $\lambda$  changes in  $W^{-1} - \mu$  parameter space. Values for the parameters are under a 95% confidence interval.

Parameter	$k_1$	$k_0$	$r_1$	$r_0$
Value	$2.5 \pm 0.14$	$-2.6 \pm 0.10$	$8.6 \pm 1.5$	$-9.1 \pm 0.96$

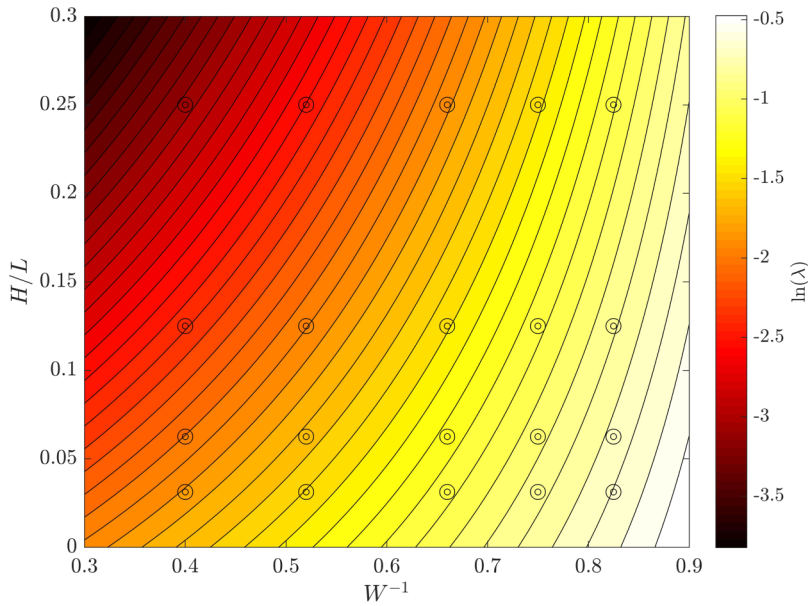


FIG. 14. How  $\lambda$  changes in  $(W^{-1}, \mu)$  parameter space. Each circle corresponds to a particular case run and where it lies in the parameter space.

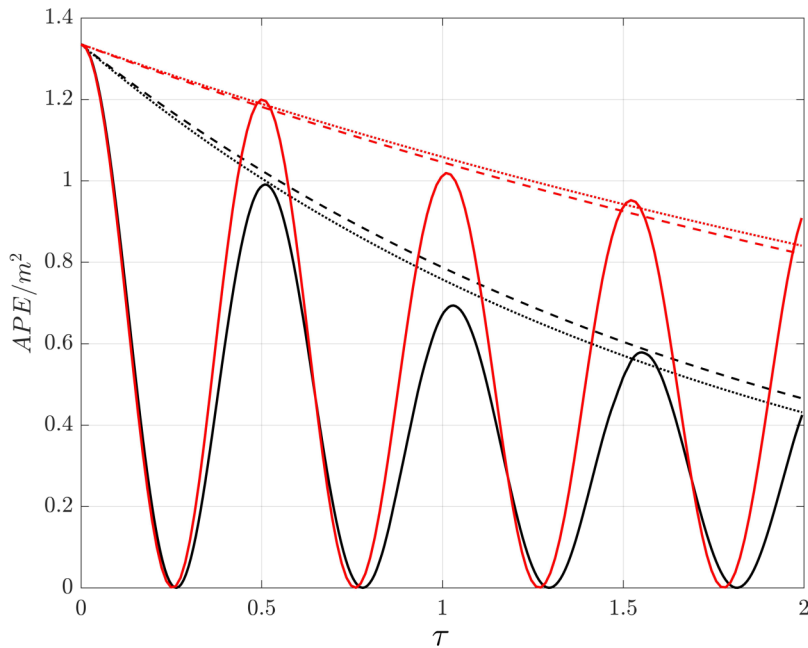


FIG. 15. Comparison of the model decay parameter (dashed line) and the calculated decay parameter (dotted line) against the mode 1 contribution to the  $E_a$  (solid line) for two cases. The 25L5-8m case is in black and the L5-2m case is in red. The oscillating component out of the model was removed because there is no decay in mode 1  $E_a$  built into the oscillating part.

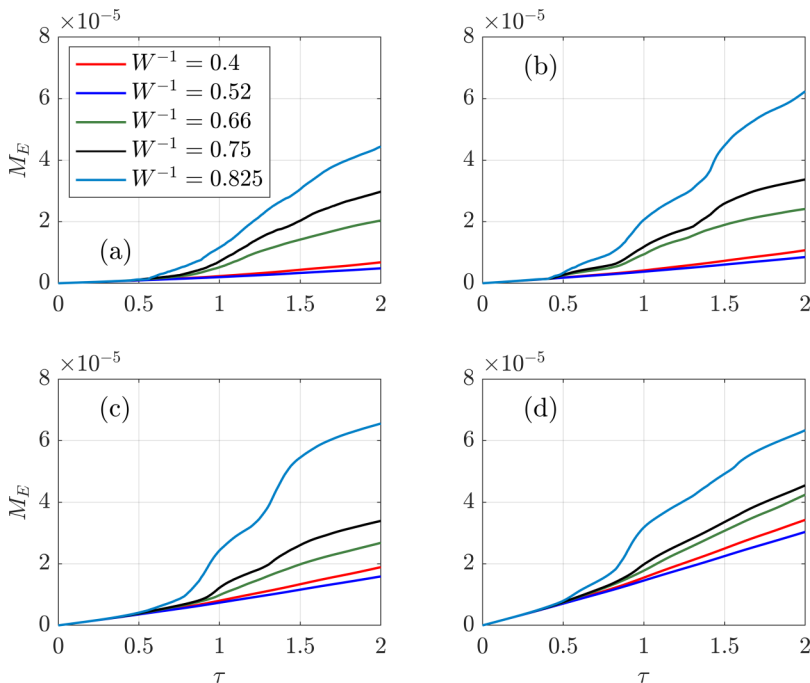


FIG. 16. The  $M_E$  time series for every case in Table I. Panels (a)–(d) show the time series for the 1-m, 2-m, 4-m, and 8-m cases respectively, with the initial dimensionless amplitude denoted by different colors.

more efficient than small-scale shear instability or localized overturning at extracting energy from the fundamental mode of the seiche. On the other hand, for all cases with constant aspect ratio, the rate at which  $E_a$  is removed from the first harmonic *increases* with increasing dimensionless amplitude. As the dimensionless amplitude becomes larger, the rate at which energy leaves the first harmonic has a weaker dependence on the aspect ratio of the wave, denoted by the clustering of the points of the aspect ratios, but as the dimensionless amplitude decreases, the variation of the rate of change of  $E_a$  is reasonably large.

The results in Fig. 12 suggest a linear dependence of  $\ln(\lambda)$  on both  $\mu$  and  $W^{-1}$ . Thus, the following model is proposed:

$$\ln(\lambda) = R_1\mu + R_0, \quad (29)$$

where  $R_1$  and  $R_0$  are constants only dependent on  $W^{-1}$ . The constants of integration are calculated via linear fits to the data and are plotted in Figs. 13(a) and 13(b). Both  $R_1$  and  $R_0$  are found to depend nearly linearly on  $W^{-1}$ . Because of the spread of the markers,  $R_0$  also depends weakly on the aspect ratio, but not enough to warrant further analysis. Since both  $R_1$  and  $R_0$  are dominated by variation  $W^{-1}$ , the fit allows for a complete closed-form model of  $\lambda(W^{-1}, \mu)$ , Eq. (29), as

$$R_0 = k_1 W^{-1} + k_2 \quad (30)$$

and

$$R_1 = r_1 W^{-1} + r_2. \quad (31)$$

The values for  $k_1$ ,  $r_1$ ,  $k_2$ , and  $r_2$  under a 95% confidence interval are presented in Table III.

Figure 14 shows how  $\lambda$  changes in parameter space and where each of the cases performed for this study lies in the model. From Fig. 14, the decay rate is seen to be lowest at high aspect ratios and low dimensionless amplitudes, which agrees with the data from Figs. 12(a) and 12(b). The

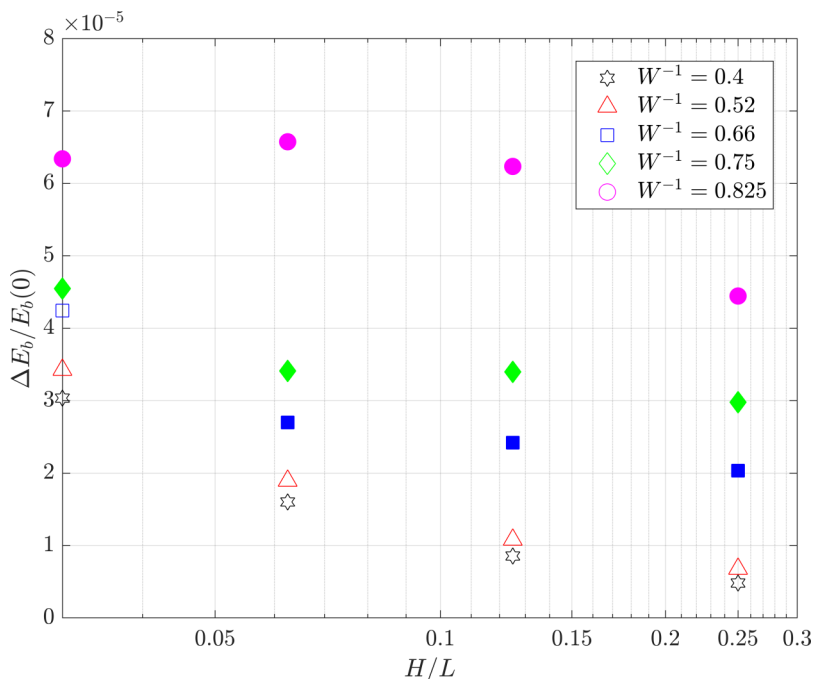


FIG. 17. The change in  $E_b$  as a percentage of the initial  $E_b$  plotted against  $\mu$ . The change in  $E_b$  is taken as the final value  $E_b$  of the fluid at  $\tau = 2$  minus the initial background potential energy of the pycnocline. The points with the same marker shape are of equal  $W^{-1}$ . Read left to right, the aspect ratios of columns of points are  $\mu = 0.03125$ ,  $\mu = 0.0625$ ,  $\mu = 0.125$ , and  $\mu = 0.25$ . Filled markers are cases where Kelvin-Helmholtz (or similar) billows are seen.

model also agrees with the notion that at high dimensionless amplitudes and low aspect ratios,  $E_a$  is extracted from the first harmonic of the seiche fastest.

Plotted in Fig. 15 (see caption for details) is the potential energy calculated via Eq. (12) and the decaying part of the model in Eq. (28) for the 25L5-8m case (black) and the L5-2m case (red). The model predicts the extraction of the mode one energy reasonable well, overestimating the decay parameter for 25L5-8m and underestimating for the L5-2m case. However, the model predicts the large-scale extraction of mode 1 energy fairly well for two fundamentally different cases.

### F. Interfacial mixing

Most cases considered in this paper exhibit mixing of fluid from the upper and lower layers, resulting in interfacial widening. For instance, at later times, Figs. 2(d), 3(d), and 7(d) show that at least part of the pycnocline has become wider due to mixing.

Figure 16 serves to show that when both shear instability and wave propagation are considered together, there are multiple mixing events, resulting in a greater increase in the  $M_E$ . These events are seen as a change in concavity of the curve. Curves of this form are shown in Ref. [47] with respect to the gain of potential energy due to KH billows and Holmboe waves. In this paper, Holmboe waves are not explicitly considered. The  $M_E$  increases for the smallest amplitude cases,  $W^{-1} = 0.4, 0.52$ , for every aspect ratio are nearly linear, and in these cases no evidence of billowing is seen. The curves for the larger amplitude cases,  $W^{-1} = 0.66, 0.75$ , and  $0.825$ , increase at a higher rate and are seen to have more than one event in many cases. The curves appear to diverge somewhere between  $\tau = 0.5$  and  $1$  after the bulk of the dispersive waves have formed. It appears that cases with multiple billowing events caused by the formation of dispersive waves increase the  $E_b$  much faster. This is

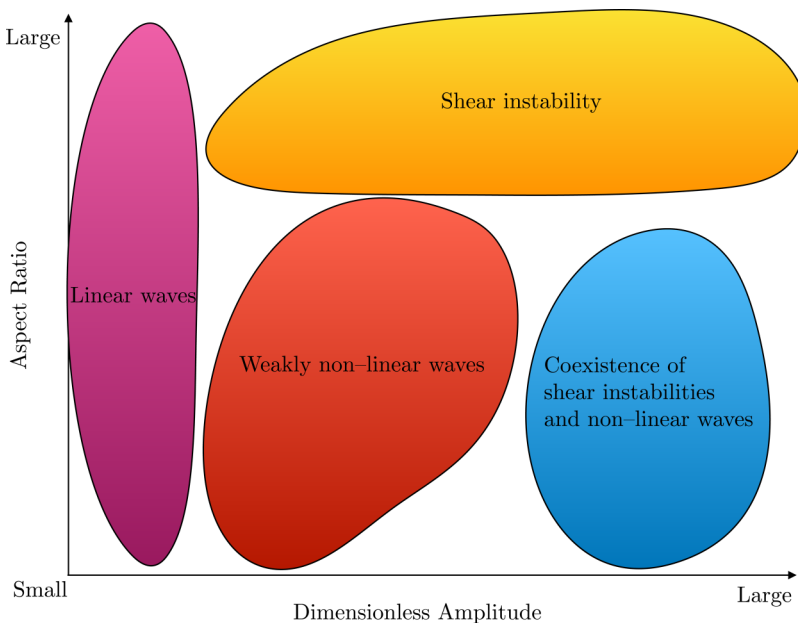


FIG. 18. A qualitative degeneration regime diagram for a laboratory-scale seiche. A “linear waves” bubble is included to show that at small amplitudes, linear theory is sufficient to predict wave motion. For large amplitude and reasonably short tanks, shear instabilities form (L5-1m, L5-2m). For midlength and midamplitude waves, wave trains form and for longer tanks with large amplitudes, both shear instabilities and wave trains form (15L5-4m, 15L5-8m, 25L5-4m, 25L5-8m).

clearly evident in the  $W^{-1} = 0.825$  case in Fig. 16(c) as the formation of billows and the subsequent interactions with the wave trains increase the  $M_E$  at a greater rate. The confound here is that the shortest cases undergo the smallest increase in the  $M_E$  due to only one instance of billowing and no clear wave formation. For the longer cases where it is possible to form a propagating wave train, there is a larger increase in the  $M_E$ .

Figure 17 shows the relative change in  $E_b$  over two periods. It is clear that it is not a simple relationship between the aspect ratio and the dimensionless amplitude of the seiche. Cases denoted by filled in markers are those for which Kelvin-Helmholtz instabilities are observed. Notice that the increase in  $E_b$  of cases without Kelvin-Helmholtz billows fall off exponentially with increasing aspect ratio. However, the cases where Kelvin-Helmholtz billows do appear do not fall off exponentially but instead appear to level off to some relatively constant value. Conversely, the character of the relative  $E_b$  increase completely changes for the case with the largest dimensionless amplitude ( $W^{-1} = 0.825$ ), denoted by magenta circles. For the cases with  $(W^{-1}, \mu) = (0.825, 0.0625)$  and  $(0.825, 0.125)$ , the interaction between shear instabilities and propagating solitary waves was seen as opposed to the case  $(W^{-1}, \mu) = (0.825, 0.25)$ , where only shear instabilities were seen.

#### IV. DISCUSSION

High-resolution pseudospectral simulations of internal seiches are performed with a focus on cases with sufficiently large dimensionless amplitude to yield either significant Kelvin-Helmholtz billows, trains of solitary like waves, or both. None of the simulations exhibit the formation of turbulent bores, and indeed most observations in lakes suggest that the formation of nonlinear wave trains (i.e., undular bores) is a far more generic phenomenon. A particular focus of the study is on the change in behavior as the aspect ratio is varied, and the way in which this change is manifested in the energetics and mixing. While the dynamics of small-amplitude waves can be described with

linear and weakly nonlinear theories [22,23], the results of this paper indicate that short tanks, or large aspect ratios, yield behavior that is dominated by shear instability that sets in near the node of the standing wave [42]. Once the instability has ceased, the oscillations are due almost exclusively to lower harmonics indicated by Fig. 11, behavior demonstrated in Horn *et al.* [18]. Increasing the tank length, or decreasing the aspect ratio, increases the rate at which the standing wave breaks down into a nonlinear wave train where higher harmonics are activated for longer times.

In many cases where the dimensionless amplitude and the length of the domain are sufficiently large, the formation of the wave train coexists with shear instabilities during the evolution, and there is enhanced mixing as the instabilities and waves interact. This is clearly apparent in the 25L5-4m case from Figs. 16(c) (light blue curve) and 17. This aspect ratio and dimensionless amplitude combination appear to allow for the largest relative change in the  $E_b$  as well as an efficient transfer of energy from the fundamental harmonic of the seiche to higher harmonics.

The dynamics discussed above are schematized in Fig. 18. Many of the cases in the present paper fall into a regime where shear instabilities and dispersive wave trains coexist.

In order to build an understanding of the energetics of the wave field, spectral analysis of the KE is utilized to build a mode-by-mode understanding of the flow. This analysis is partially based off of the analysis performed by Horn *et al.* [18]. Where they use an *a priori* method of estimating when the nonlinearity of the system becomes important, an *a posteriori* method based on spectral decomposition of the KE is used here. Nonlinear effects become important when higher harmonics become excited due to various mechanisms. With the cases discussed in the second section of this paper, it is found that the development of a solitary wave occurs very rapidly in the evolution of the seiche when the layer depths are unequal. This evolution is heuristically predicted by weakly nonlinear wave theory (the KDV equation and variants discussed by Helfrich and Melville [22]) and agrees qualitatively with the results developed by Horn *et al.* [18]. Many of the cases not discussed also undergo a rapid transition from large-scale oscillation to small-scale wave activity before the first half period. To compare, most of the cases considered in Ref. [18] fall into a regime in which the dominant degeneration mechanism is the formation of a packet of solitary waves.

To complement the analysis for the KE, a semianalytical model is developed which gives an estimate as to the rate at which  $E_a$  is irreversibly removed from the fundamental mode of the seiche. This rate is not indicative of the energy lost to dissipative forces and mixing, but instead gives an indication as to how fast energy is extracted from the fundamental mode of the seiche. Though viscosity is not explicitly accounted in this analysis, at early times, the model is reasonably representative of the rate at which  $E_a$  is extracted from the fundamental mode of the seiche. The results of this model quantify the fact that the  $E_a$  leaves the fundamental mode faster for cases with a larger dimensionless amplitude and slower for a smaller dimensionless amplitude. This agrees with the qualitative results from Figs. 2, 3, and 7 as well as with the analysis of Horn *et al.* [18] and Boegman *et al.* [20]. This model is *not* meant to be a replacement for the more correct stratified case.

This paper also includes a quantitative analysis of fluid mixing. The paradigm that Figs. 16 and 17 demonstrate is that shear instabilities and solitary waves can coexist and enhance the amount of mixing that occurs. Figure 16 shows that when only shear instabilities are allowed to form there is typically one mixing event, where in cases where propagating waves occur, there are multiple. This contrast is seen by comparing the time series in Fig. 16(a) to Figs. 16(c) or 16(d).

With a higher dimensionless amplitude, there is a larger initial input of  $E_a$ . This energy can be transferred to KE and back to  $E_a$  (which results in oscillations of the density interface), it can be transferred to KE and dissipated, or fluid layers can be mixed, resulting in an increase of  $E_b$  [34]. However, if the dimensionless amplitude is not large, the results from Fig. 14 suggest that the rate at which  $E_a$  is exacted from the fundamental mode of the seiche is small and therefore there is less energy for mixing.

There are several directions in which this research could be continued. One is by resolving the boundary layer dynamics. Because the viscosity is small, boundary layers are thin, and solving the Navier-Stokes equations including the boundary becomes a problem with multiple scales. Thus,

points must be clustered near boundaries in order to resolve any motion at those scales. What the model in Eq. (28) does not take into account and might be of interest for future work is the effect that the boundary has on the large-scale dynamics of the flow and its energetics. By resolving the boundary layer, one could build an understanding of how the viscous dissipation at the boundary affects the dynamics of the large-scale flow. It should be expected that by resolving the boundary layer, mechanical energy is explicitly removed due to dissipation, and this in turn damps the wave motion. Complex situations involving boundary separation and intrusion of near-boundary fluid into the main water column may also be possible and merit exploration. As well, in the field, it is known that the motion resulting from a seiche can contribute to the vertical transport of matter and biological material [9], so by utilizing high-resolution simulations of seiche boundary layers, parametrizations of vertical transport of material could be created and used in larger scale models.

Another direction in which this research could be taken is building an understanding of the full three-dimensional dynamics in high resolution. The scales that are considered in this paper are comparable to length scales found in a laboratory; thus, it is not unreasonable to expect three-dimensional dynamics to occur. These dynamics could possibly allow for slightly different energetics as well as differences in mixing dynamics. Some representative cases discussed in this paper could be performed in three dimensions to see if the bulk dynamics change during the transition to turbulence. By performing simulations in three dimensions, secondary instabilities and true transition to turbulence can occur, as in the well-documented studies of shear instability by Peltier and Caulfield [40], Mashayek and Peltier [48], and Mashayek and Peltier [49]. We discussed earlier that these shear instabilities are important for the mixing of the fluid; hence by accurately resolving their three dimensional aspects, a better quantitative understanding of the interfacial mixing could be built.

In terms of experiment, further steps include verifying the analysis and results of the  $E_a$  decay rate. This can help to verify whether or not these parametrizations can be included in field-scale models. Currently, the majority of field-scale models would not be able to accurately resolve the nonhydrostatic aspects of the fluid flow that contribute to the irreversible change of  $E_a$ .

#### ACKNOWLEDGMENTS

The authors thank the two anonymous referees for the helpful comments that improved the quality of this paper. This work was funded by the Natural Sciences and Engineering Research Council of Canada, in the form of Grant No. RGPIN-311844-37157.

- 
- [1] B. Boehrer and M. Schultze, Stratification of lakes, *Rev. Geophys.* **46**, 1 (2008).
  - [2] E. R. Watson, Movements of the waters of Loch Ness, as indicated by temperature observations, *Geogr. J.* **24**, 430 (1904).
  - [3] A. Wüest and A. Lorke, Small scale hydrodynamics in lakes, *Annu. Rev. Fluid Mech.* **35**, 373 (2003).
  - [4] I. Ostrovsky, Y. Z. Yacobi, P. Walline, and I. Kalikhman, Seiche-induced mixing: Its impact on lake productivity, *Limnol. Oceanogr.* **41**, 323 (1996).
  - [5] L. Boegman, J. Imberger, G. N. Ivey, and J. P. Antenucci, High-frequency internal waves in large stratified lakes, *Limnol. Oceanogr.* **48**, 895 (2003).
  - [6] M. Preusse, F. Peeters, and A. Lorke, Internal waves and the generation of turbulence in the thermocline of a large lake, *Limnol. Oceanogr.* **55**, 2353 (2010).
  - [7] M. Preusse, M. Stastna, H. Freistühler, and F. Peeters, Intrinsic breaking of internal solitary waves in a deep lake, *PLoS ONE* **7**, e41674 (2012).
  - [8] M. Preusse, H. Freistühler, and F. Peeters, Seasonal variation of solitary wave properties in Lake Constance, *J. Geophys. Res.: Oceans* **117**, 1 (2012).

- [9] S. MacIntyre, K. M. Flynn, R. Jellison, and J. R. Romero, Boundary mixing and nutrient fluxes in Mono Lake, California, *Limnol. Oceanogr.* **44**, 512 (1999).
- [10] S. M. Henderson and B. R. Deemer, Vertical propagation of lakewide internal waves, *Geophys. Res. Lett.* **39**, 2 (2012).
- [11] S. M. Henderson, Turbulent production in an internal wave bottom boundary layer maintained by a vertically propagating seiche, *J. Geophys. Res. [Oceans]* **121**, 2481 (2016).
- [12] B. R. Deemer, S. M. Henderson, and J. A. Harrison, Chemical mixing in the bottom boundary layer of a eutrophic reservoir: The effects of internal seiching on nitrogen dynamics, *Limnol. Oceanogr.* **60**, 1642 (2015).
- [13] A. Dorostkar, L. Boegman, and A. Pollard, Three-dimensional simulation of high-frequency nonlinear internal wave dynamics in Cayuga Lake, *J. Geophys. Res. [Oceans]* **122**, 2183 (2017).
- [14] P. Brandt, A. Rubino, W. Alpers, and J. O. Backhaus, Internal waves in the Strait of Messina studied by a numerical model and synthetic aperture radar images from the ERS 1/2 satellites, *J. Phys. Oceanogr.* **27**, 648 (1997).
- [15] A. de la Fuente, K. Shimizu, J. Imberger, and Y. Niño, The evolution of internal waves in a rotating, stratified, circular basin and the influence of weakly nonlinear and nonhydrostatic accelerations, *Limnol. Oceanogr.* **53**, 2738 (2008).
- [16] D. T. Steinmoeller, M. Stastna, and K. G. Lamb, Fourier pseudospectral methods for 2D Boussinesq-type equations, *Ocean Model.* **52**, 76 (2012).
- [17] D. T. Steinmoeller, M. Stastna, and K. G. Lamb, Pseudospectral methods for Boussinesq-type equations in an annular domain with applications to mid-sized lakes, *J. Comp. Sci.* **4**, 3 (2013).
- [18] D. A. Horn, J. Imberger, and G. N. Ivey, The degeneration of large-scale interfacial gravity waves in lakes, *J. Fluid Mech.* **434**, 181 (2001).
- [19] D. A. Horn, J. Imberger, G. N. Ivey, and L. G. Redekopp, A weakly nonlinear model of long internal waves in closed basins, *J. Fluid Mech.* **467**, 269 (2002).
- [20] L. Boegman, G. N. Ivey, and J. Imberger, The energetics of large-scale internal wave degeneration in lakes, *J. Fluid Mech.* **531**, 159 (2005).
- [21] K. G. Lamb, Are solitary internal waves solitons? *Stud. Appl. Math.* **101**, 289 (1998).
- [22] K. R. Helfrich and W. K. Melville, Long nonlinear internal waves, *Annu. Rev. Fluid Mech.* **38**, 395 (2006).
- [23] P. K. Kundu, I. Cohen, and D. Dowling, *Fluid Mechanics*, 5th ed. (Elsevier, Amsterdam, 2012).
- [24] D. J. Korteweg and G. de Vries, On the change of form of long waves advancing in a rectangular canal, and on a new type of long stationary waves, *Philos. Mag. Ser. 5* **39**, 422 (1895).
- [25] J. W. Miles, The Korteweg–de Vries equation: A historical essay, *J. Fluid Mech.* **106**, 131 (1981).
- [26] C. J. Subich, K. G. Lamb, and M. Stastna, Simulation of the Navier-Stokes equations in three dimensions with a spectral collocation method, *Int. J. Numer. Methods Fluids* **73**, 103 (2013).
- [27] D. Deepwell, M. Stastna, and A. Coutino, Multi-scale phenomena of rotation-modified mode-2 internal waves, *Nonlinear Processes Geophys.* **25**, 217 (2018).
- [28] A. Coutino and M. Stastna, The fully nonlinear stratified geostrophic adjustment problem, *Nonlinear Processes Geophys.* **24**, 61 (2017).
- [29] J. Olsthoorn and S. B. Dalziel, Vortex-ring-induced stratified mixing: Mixing model, *J. Fluid Mech.* **837**, 129 (2018).
- [30] A. Coutino, M. Stastna, S. Kovacs, and E. Reinhardt, Hurricanes Ingrid and Manuel (2013) and their impact on the salinity of the meteoric water mass, Quintana Roo, Mexico, *J. Hydrol.* **551**, 715 (2017).
- [31] E. Bembenek, F. J. Poulin, and M. L. Waite, Realizing surface-driven flows in the primitive equations, *J. Phys. Oceanogr.* **45**, 1376 (2015).
- [32] B. A. Storer, F. J. Poulin, and C. Ménesguen, The dynamics of quasi-geostrophic lens-shaped vortices, *J. Phys. Oceanogr.* **48**, 937 (2017).
- [33] K. G. Lamb and L. Yan, The evolution of internal wave undular bores: Comparisons of a fully nonlinear numerical model with weakly nonlinear theory, *J. Phys. Oceanogr.* **26**, 2712 (1996).
- [34] K. B. Winters, P. N. Lombard, J. J. Riley, and E. A. D’Asaro, Available potential energy and mixing in density-stratified fluids, *J. Fluid Mech.* **289**, 115 (1995).

- [35] W. H. Press, *Numerical Recipes in C: The Art of Scientific Computing* (Cambridge University Press, Cambridge, UK, 1992).
- [36] K. B. Winters and E. A. D'Asaro, Diascalar flux and the rate of fluid mixing, *J. Fluid Mech.* **317**, 179 (1996).
- [37] K. G. Lamb and V. T. Nguyen, Calculating energy flux in internal solitary waves with an application to reflectance, *J. Phys. Oceanogr.* **39**, 559 (2009).
- [38] R. Salmon, *Lectures on Geophysical Fluid Dynamics*, 1st ed. (Oxford University Press, New York, 1998), p. 378.
- [39] A. Scotti and B. White, Diagnosing mixing in stratified turbulent flows with a locally defined available potential energy, *J. Fluid Mech.* **740**, 114 (2014).
- [40] W. R. Peltier and C. P. Caulfield, Mixing efficiency in stratified shear flows, *Annu. Rev. Fluid Mech.* **35**, 135 (2003).
- [41] K. M. Thyng, C. A. Greene, R. D. Hetland, H. M. Zimmerle, and S. F. DiMarco, True colors of oceanography: Guidelines for effective and accurate colormap selection, *Oceanogr.* **29**, 9 (2016).
- [42] S. A. Thorpe, On standing internal gravity waves of finite amplitude, *J. Fluid Mech.* **32**, 489 (1968).
- [43] J. Grue, A. Jensen, P.-O. Rusås, and J. K. Sveen, Properties of large-amplitude internal waves, *J. Fluid Mech.* **380**, 257 (1999).
- [44] M. F. Barad and O. B. Fringer, Simulations of shear instabilities in interfacial gravity waves, *J. Fluid Mech.* **644**, 61 (2010).
- [45] M. Carr, S. E. King, and D. G. Dritschel, Numerical simulation of shear-induced instabilities in internal solitary waves, *J. Fluid Mech.* **683**, 263 (2011).
- [46] C. D. Troy and J. R. Koseff, The instability and breaking of long internal waves, *J. Fluid Mech.* **543**, 107 (2005).
- [47] W. D. Smyth and K. B. Winters, Turbulence and mixing in Holmboe waves, *J. Phys. Oceanogr.* **33**, 694 (2003).
- [48] A. Mashayek and W. R. Peltier, The “zoo” of secondary instabilities precursory to stratified shear flow transition, part 1: Shear aligned convection, pairing, and braid instabilities, *J. Fluid Mech.* **708**, 5 (2012).
- [49] A. Mashayek and W. R. Peltier, The “zoo” of secondary instabilities precursory to stratified shear flow transition, part 2: The influence of stratification, *J. Fluid Mech.* **708**, 45 (2012).